Relationship between design strategies of commercial three-way monolithic catalysts and their performances in realistic conditions

Shreya Nandi, Paola-Beatriz Arango Ponton, Christophe Chaillou, Christophe Dujardin, Pascal Granger, Emmanuel Laigle, André Nicolle, Caroline Norsic, Mélissandre Richard

Relationship Between Design Strategies of Commercial Three-way Monolithic Catalysts and their Performances in Realistic Conditions

Shreya Nandi[a], Paola Arango[a], Christophe Chaillou[b], Christophe Dujardin[a], Pascal Granger[a], Emmanuel Laigle[b], André Nicolle[b], Caroline Norsic[c*], Melissandre Richard[a*]

[a] Univ. Lille, CNRS, Centrale Lille, Univ. Artois, UMR 8181 – UCCS – Unité de Catalyse et Chimie du Solide, F-59000 Lille, France
[b] Aramco Fuel Research Center, 232 Avenue Napoleon Bonaparte, 92852 Rueil-Malmaison, France
[c] EMC France, 4 Allée de la rhubarbe, Achères, 78260, France

* Corresponding authors:
Melissandre Richard ; E-mail Address : melissandre.richard@centralelille.fr
Caroline Norsic ; E-mail Address : caroline.norsic@emcfrance.fr

Abstract

Monolith-shaped three-way catalysts (TWC) are always at the edge of science and technology as a response to the stringent updates on the emission standards worldwide. In spite of rapid research on TWC materials, the exact compositions adapted by major automotive companies are not fully known. This study focuses on comparing two fresh commercial monolithic catalysts for gasoline engines, namely, monolith-A and monolith-B, to highlight the significance of their manufacturing strategies by its characterization and catalytic evaluation under realistic lean/rich/stoichiometric regimes. Firstly, monolith-A demonstrates a zoning on its front and back side with high Pd and Rh loading to enhance CO/HC oxidation and NO_x reduction, respectively, having higher amounts of trace dopants like La, Y, Pr and S. Whereas, monolith-B has a homogeneous composition with much lower noble metal/trace elements content without any Pr and S. Secondly, the double-layer washcoating is employed by following different routes with distinct compositions of alumina and ceria-zirconia. Monolith-B showed better low temperature CO oxidation performance while monolith-A performed better for NOx reduction owing to higher Rh loading. Overall, the zoning strategy of monolith-A raises question on its cost effectiveness in regards to its performance while poor reduction capabilities is exhibited by monolith-B. This study highlights that the latest TWC strategies have a scope of further development particularly with respect to the catalytic performance/expense ratio.

Keywords

Three-way catalysis, Monolithic Catalyst, Commercial Strategies, Washcoat, Emission control

1. Introduction

All over the world, emissions of carbon monoxide (CO), unburned hydrocarbons (HC), nitrogen oxides (NO_x) and particulate matter (PM) are regulated for most vehicle types, leading the automotive industries to the development of catalytic converters for reducing such emissions [1]. As environmental regulations become more stringent all over the world (Euro 6d, China 6a, California LEVIII and Federal United States Tier 3 standards), increasingly efficient catalytic and sorbent formulation and/or design must be found to meet their objectives in future vehicles [2,3]. The advanced three-way catalysis (TWC) technology, currently implemented in gasoline vehicles, allows simultaneous abatement of CO, NO_x and HC near stoichiometric air-to-fuel ratio (λ values) [4,5]. Commercial catalysts are based on active metallic phases from Platinum Group Metals (PGMs). Platinum and palladium are suitable for CO and HC oxidation while rhodium is used for NO_x reduction to N_2 [6]. Usually, metals are supported on a washcoat containing a mixture of (i) cerium-zirconium based oxides primarily due to their oxygen storage capacity (OSC) and resistance to thermal sintering [7-11], and (ii) γ-alumina for its high surface area and thermal stability [12,13]. Numerous rare earth and alkaline promoter materials such as La, Nd, Pr, Sm, Y, Ba or Sr can be added to the washcoat to further improve thermal stability and OSC performances [13-17]. Monolith-shaped cordierite substrates with hexagonal or square channels are largely used to support the metal/washcoat catalysts to ensure merely hydrodynamics limiting the back-pressure and improve mass transfer and thermal/mechanical stability [18]. Recent advances in fuel economy leads to a significant challenge in enhancing low temperature performance of the catalyst to perform pollutant conversion during cold-start phases [19]. Indeed, up to 80% of tailpipe emissions may occur during the starting-up period, especially in urban areas, when the catalyst does not reach its light off temperature yet [20]. The development of more efficient technologies can lead to significant emission reduction. However, that demands a complete understanding of the catalyst formulation and design related to its conversion efficiency. Among others, recent studies focused on washcoat composition [21], metal/metal [22] and metal/$Ce_xZr_{1-x}O_2$ [23] interactions showing multifaceted relationship with catalytic performances, which remain to be fully understood.

As an ambitious objective of developing a neutral air quality impact vehicle, we investigated the catalytic strategies of two different automotive companies to reach the present emission standards. In particular, cordierite support design, metal loadings, ratios and distribution along the monoliths are carefully considered. We focused on washcoat formulation using a variety

of the characterization methods including X-Ray fluorescence (XRF), photoelectron (XPS) and diffraction (XRD) spectroscopies, scanning electron microscopy (SEM), N_2 physisorption and temperature programmed reduction under hydrogen (H_2-TPR), in regard to the catalytic performance for CO and propane/propene oxidation as well as NO reduction with CO. A specific lab-scaled set-up was developed to evaluate and compare catalytic efficiencies of both commercial materials under realistic conditions, particularly with change between rich/stoichiometric/lean regimes.

2. Materials and methods

2.1. Sample selection and characterization

The fresh samples of commercial monolithic TWCs of unknown composition from two different automotive manufacturers were used. The selected monoliths for the current study are named, monolith-A and monolith-B, for confidentiality reasons. To maintain homogeneity of chemical composition, the monolith samples have been cut from the front-side of the installed TWC in cylindrical shapes. Each sample is 6.1 cm in length with a diameter of 1.35 ± 0.05 cm. The monoliths have been directly used for catalytic testing and crushed to form a powder for characterizations, whenever necessary.

X-ray fluorescence (XRF) analysis was carried out using a wavelength dispersive X-ray fluorescence S2 Ranger Bucker spectrometer equipped with a palladium tube to identify the elemental composition of the catalysts. The powdered catalyst with a mass of 500 mg was used for the analysis in a closed vessel with an X-ray transparent mylar film.

Powder X-ray diffraction (XRD) analysis was carried out at room temperature on a Bruker AXS D8 Advance diffractometer in the Bragg–Brentano geometry using a Cu Kα source (λ = 0.154 nm). The diffraction pattern was recorded in in 2θ range 5-80° with a step size of 0.05°, 1 second per step scan ranging from $5° < 2\theta < 80°$.

The Scanning electron microscopy (SEM) analysis was performed with a Hitachi S4700 microscope, Japan at 15 kV. The sample was cut and put within a polymer resin to facilitate the analysis of the monolith cross-section. It was then polished and carbon coated to minimize any charging issues.

The X-ray photoelectron spectroscopy (XPS) analysis was carried out using an AXIS Ultra DLD Kratos spectrometer equipped with a monochromatic aluminum Kα source at 1486.6 eV with pass energy of 40 eV at 10^{-10} mbar. Charge compensation was applied to neutralize any

charging effects. All binding energies were calibrated with respect to the C 1s spectrum of adventitious carbon at 285 eV. The data analysis was performed using CasaXPS software. Hydrogen-temperature programmed reduction (H_2-TPR) measurements were made on a Micromeritics AutoChemII 2920 instrument. During the analysis, 200 mg of powder sample was pretreated in a 20 mL.min^{-1} flow of Argon up to 150 °C for 1 hour and then cooled to room temperature. The reduction was then performed with a 20 mL.min^{-1} flow of 5 Vol% H_2/Ar. The hydrogen consumption was monitored with a heating ramp of 10 °C.min^{-1} up to 1000 °C using a thermal conductivity detector. Any water produced was trapped in a cold trap before reaching this detector. The TPR was additionally performed directly on the monolith shaped sample. A dynamic gas sorption analyzer was used coupled to a mass spectrometer (IGA-003 Dynamic Gas Sorption Analyzer, Hiden Isochema). Here, a sample of approximately 1 g was cut from monolith and was analyzed under the same conditions as used for the powder samples.

Nitrogen physisorption measurements were performed at -196 °C on a Micromeritics FlowSorbIII. The specific surface area was determined using 0.2 g of powder sample, previously outgazed at 150 °C under vacuum for 2 h. Brunauer-Emmett-Teller (BET) theory was applied to calculate the specific surface areas. Pore size distributions were obtained at the same time from the isotherms based on the Barret-Joyner-Halenda (BJH) theory.

2.2. Catalytic performance measurements

The catalytic setup was built according to the scheme shown in Fig. S1 of the supplementary information (SI) for evaluating the catalyst performances in different TWC regimes during a single experimental run. The setup was thereby equipped with two solenoid valves to feed an oxygen/helium mixture at different concentration for maintaining the lean, rich or stoichiometric condition. A homemade timer (Crouzet Millenium 3) allowed controlling the switching of valves across the different regimes every 15 minutes. The different reactant gases (CO, NO, propane/propene from AirLiquid) as well as O_2/He flow rates were controlled by a digital control unit attached to the mass flow controllers. The stainless steel reactor enabled to directly hold a monolith-shaped catalyst with a maximum diameter of 1.4 cm and a maximum height of ~10 cm. The reactor was placed in an oven using a temperature controller (West N6400). An additional thermocouple was used to record real-time temperature of the monolithic sample. A Peltier water trap and a genie filter allowed further removal of water and protect the analyzers from contaminants. The gases from the reactor outlet were finally

analyzed during the reaction with μGC (Double channel Agilent 3000), infrared (Industrial Gas Analyzer de (IGS) Antaris^{TM}, Thermo Scientific) and chemiluminescence (MIR 9000 Multigas analyzer, Envea) detectors, simultaneously.

Different reactions including CO oxidation by O_2 and/or NO and propene-propane oxidation were investigated. Note that propene was chosen as model alkene molecule to mimic realistic exhaust composition measured from multiple Euro6d temp gasoline engines where propene and acetylene were found in small amounts (500 and 100 ppmv, respectively). Other pollutants such as CH_4, pentane(s) as well as H_2 were detected in that gas exhaust and are the subject of a complementary study not reported in this paper. The concentrations of the reactants under rich-lean-stoichiometric regimes have been given in Table S1. The λ values varied in the range of 0.5-1.5 to comprehend each regime's significance for a specific reaction with a total flow of 1 L min^{-1} (at 20 °C, 1 atm) and a GHSV of about 18 000 h^{-1} (based on the solid volume of the monolith reported in Table 1).

The protocol for the catalytic performance testing is described in Fig. S2(a), the catalysts were degreened to gain hydrothermal and structural stability by exposure to an atmosphere of 10% O_2 and 10% H_2O in helium for 4 hours at 500 °C with a flow rate of 1 L.min^{-1} and kept under helium at 300 mL.min-1 during cooling down to 100 °C. During the catalytic tests, the experimental protocol consists of 5 isothermal steps at every 100 °C up to 500 °C, where the regimes (lean/rich/stoichiometric) change every 15 minutes after thermal stabilization (Fig. S2(b)). Oxygen Storage Capacity (OSC) properties of the catalysts were estimated from catalytic experimental data at each temperature with respect to the ceria-zirconia content as described in supplementary material (Fig. S5).

3. Results and discussion

3.1 Catalyst morphology

The two monolithic cylinders illustrated in Fig. 1 have been investigated. The dimensions related to these monolithic catalysts are given in Table 1. The ceramic support in monolith-A consists of hexagonal channels while monolith-B shows square channels, with cell density of 319 and 352 cpsi, respectively. Both consist of double-washcoat layers over the monolithic support shown by the different contrast in their SEM images (see Fig. 1(c) and (d)). The thickness of washcoats 1 and 2 as well as the channel openings are similar for both, except for the monolith support thickness that is larger for monolith-A. The total washcoat thickness

ranges between 90 and 120 µm approximately with an open frontal area of ~60%. The main difference lies in the existence of two distinct zone coating along the monolith for monolith-A instead of one for monolith-B.

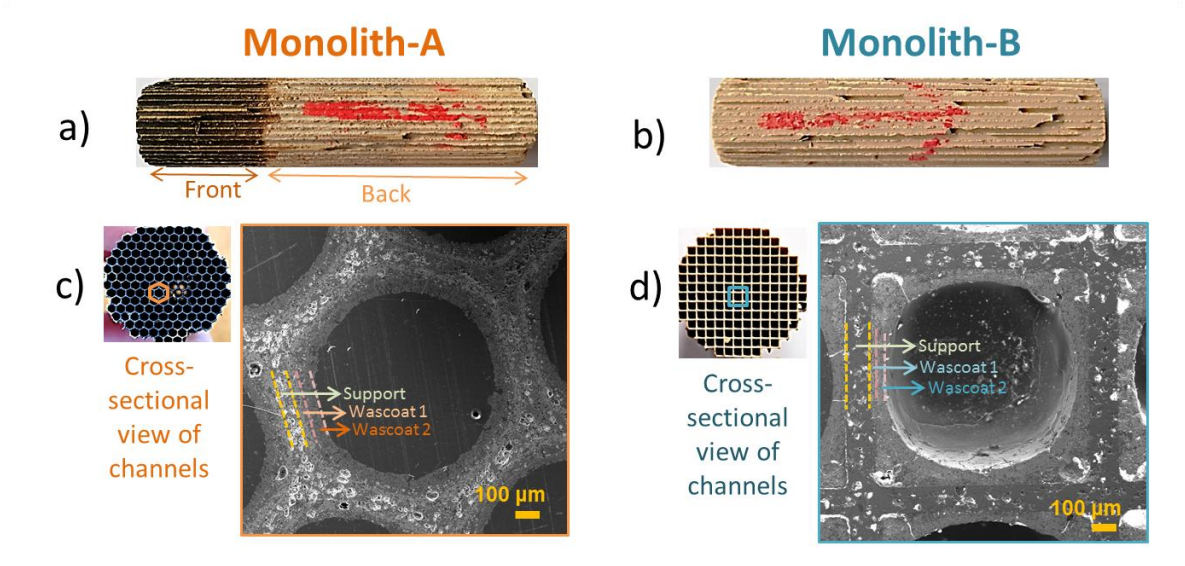

Fig. 1. (a) Monolith-A with zoned washcoating on the front and back side, (b) monolith-B with homogeneous washcoating and the SEM images with view of an individual channel of each, respectively ((c) and (d)).

Table 1. Comparison of dimensions of different parts in monolith-A and monolith-B.

	Monolith-A	**Monolith-B**
Channel shape	Circular	Square
Open frontal area	63 %	62 %
Solid volume	3.14 cm^3	3.23 cm^3
Open channel diameter	0.84 ± 0.01 mm	0.87 ± 0.02 mm
Monolithic support thickness	86.5 ± 2.4 µm	125.6 ± 8.8 µm
Thickness of Washcoat-1	55.6 ± 1.1 µm	59.3 ± 12.1 µm
Thickness of Washcoat-2	43.3 ± 1.4 µm	45.7 ± 4.6 µm

3.2 Chemical composition and structural properties

The elemental compositions have been analyzed by XRF and ICP-OES analysis on the front and back zones of monolith-A. On the other hand, monolith-B has been analyzed globally without distinction. The data in Table 2 reveal complex composition. Nevertheless, some elements included in the composition of the washcoat have more importance recognized by their high oxygen storage capacity especially when combined in solid solutions, i.e. Ce and Zr

[3]. The values of the Ce/Zr ratio varies from 0.38 in the front side of monolith-A to 0.23 in the back side of monolith-A. Strong deviations are also observable on Pd content, abnormally high on the front side of monolith-A compared to the back side as well as on monolith-B which exhibits the lowest composition. Rh loading seems to be very low and the related accuracy is likely to be poor. An unexpected observation is undoubtedly related to the presence of significant amount of sulphur on the monolith-A, whereas its absence is evident in monolith-B.

Table 2. Elemental composition of monolith-A (front and back) and monolith-B as analyzed by XRF.

Elements	**Monolith-A Front (atom%)**	**Monolith-A Back (atom%)**	**Monolith-B (atom%)**
Support:			
Si	5.44	1.28	7.46
Al[#]	16.40	14.65	13.69
Mg	5.66	6.30	3.80
Fe	0.55	0.19	0.64
Washcoat(s):			
Ce	1.50	2.14	1.83
Zr	3.96	9.16	6.84
La	2.78	0.97	0.62
Nd	-	0.30	0.47
Pr	0.66	0.08	-
S	1.71	0.92	-
Ba	0.65	0.58	0.72
Y	0.23	0.60	0.11
Rh	0.01	0.07	0.03
Pd*	1.85	0.39	0.17

* from ICP-OES
[#] Present in washcoat also

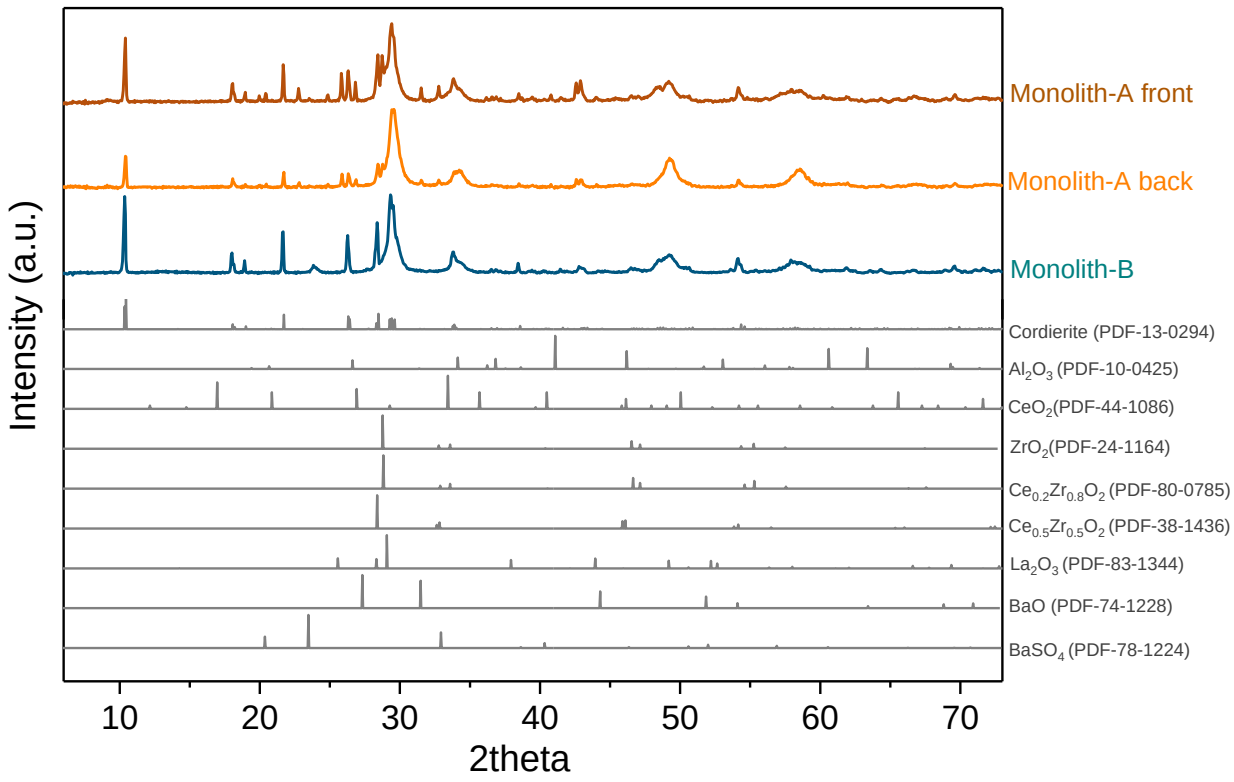

Fig. 2. XRD pattern of the crushed monoliths compared to the cordierite support and other reference oxides.

Fig. 2 illustrates XRD patterns recorded on the different samples. They are dominated by different reflections characteristic of the cordierite. However, additional reflections appear at 2θ = 20.5°, 22.9°, 23.8°, 25.0°, 27.1°, 31.8° with broad signals centered at 49.2° and 58.4°. Assignments have been attempted based on the elemental composition given in Table 2. The reference XRD patterns for the cubic CeO_2, tetragonal ZrO_2 and mixed $Ce_xZr_{1-x}O_2$ oxides in agreement with the estimated Zr/Ce have ratio have been compared. As seen in Fig. 2, the broad peaks seem to coincide with the washcoat constituents including alumina, ceria-zirconia single as well as mixed oxides. In spite of the high complexity of the XRD spectra as a result of the mixing of several phases of the washcoats, it hints at the presence of La_2O_3, barium oxide and/or sulphate (only in monolith-A) given by the comparison of their XRD patterns with respect to the monoliths.

Unlike X-ray diffraction analysis, SEM-EDX analysis provides useful information because the chemical mapping informs about the gradients in composition across the washcoat layers. Hence, homogeneous distribution of the elements and/or strong heterogeneities can be evidenced though this examination. The washcoat layers are composed of alumina for providing thermal stability and high specific surface area as well as single and/or mixed ceria-

zirconia metal oxides for imparting OSC properties in different concentrations across the two layers [7-12]. This can be observed from the SEM-EDX chemical mapping images illustrated in Fig. 3. The first washcoat layer in monolith-A is Zr-riched. On the contrary, the second washcoat seems to reveal a slightly Ce-enriched chemical environment. Another important information is related to the significant heterogeneities related to the segregation particles. In contrast for monolith-B, both the washcoat layers are more homogeneous in composition with a random distribution of Ce and Zr. Let us note that the second layer exhibits higher Zr concentration. Here small physically blended alumina particles are still present in both layers with higher concentration in the first washcoat. As evident in monolith-A, the primary metal oxide is often blended with the other in each of the washcoat layers. This kind of preparation with the presence of alumina particles in ceria-zirconia mixed oxide layer causes a diffusion barrier thereby decreasing its sintering effect at high temperatures while the presence of ceria-zirconia particles within alumina helps to preserve the efficient γ-alumina phase [24]. The homogeneous $Al_2O_3/CeO_2/ZrO_2$ mixed oxide observed in monolith-B can be obtained after simultaneous co-precipitation of all three metallic precursors. A recent study showed remarkable thermal stability and catalytic performances at low temperature for such Pd-based materials [25].

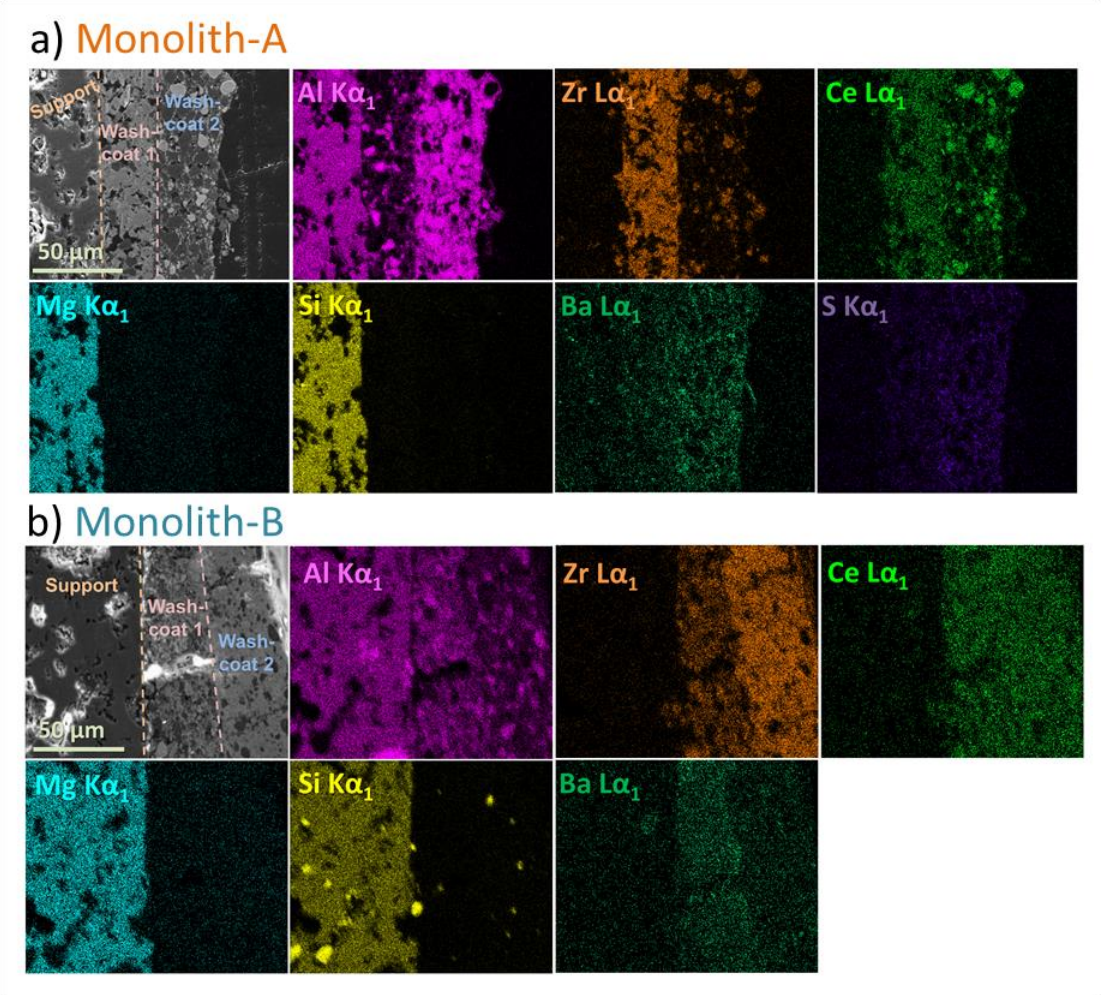

Fig. 3. SEM-EDX chemical mapping images of the washcoated layers of a) monolith-A (back) and b) monolith-B performed on the respective monolith cross-sections.

The cerium to zirconium ratio in the washcoat can also significantly impact the catalytic performances by controlling the OSC properties [11]. The Ce/Zr ratio at the surface and bulk of the powdered monoliths as determined by XPS and XRF spectroscopy, respectively, have been presented in Table 4. Both the commercial catalysts show around 40% Ce content within the overall washcoat layers for potentially retaining decent capacity of oxygen storage. It was shown in multiple studies on ceria zirconia mixture that the maximum OSC is kept between 35% to 65% of zirconia content [11, 26]. Zr-rich mixture are generally used to avoid sintering and encapsulation of PGM at high temperature [27]. Regarding the presence of sulphur for monolith-A (see Table 1), chemical mapping reveals that S is more concentrated in the washcoat 2. It is worthwhile to note that this zone seems to be Ba-enriched suggesting that it could be stabilized as barium sulphate.

The presence of additional promoters such as La, Ba and Y are also detected in both the monoliths but in higher concentration for monolith-A (Table 2). However, trace dopants like Nd is only present in monolith-A(back) and monolith-B while Pr is detected in monolith-A only. Such promoters (La, Nd, Pr, Y) are often added in trace amounts in ceria-zirconia to enhance the thermal stability and/or their OSC properties [3, 14, 28]. Ba oxide increases the reducibility and activity of the catalyst by stabilization of the alumina and improving the oxygen mobility and thermal stability of ceria-zirconia present within the washcoat [29,30]. Here, monolith-A shows high Ba content in washcoat-2 while monolith-B in washcoat-1 (Fig. 3). Finally, in regards to the active species within the monolith washcoats, PGM metals like Pd and Rh only were detected. The front side of monolith-A comprised of very high Pd loading of 1.8% while the back side was the richest in Rh at 0.07%. In general, the Pd content was higher on monolith-A irrespective of the zone compared to monolith-B at only 0.16%, whereas it contained an intermediate Rh content of 0.03%. The strategy of zoning adopted for the monolith-A allowed to deposit varying quantities of the noble metals in length with relatively high concentration of noble metals compared to monolith-B.

3.3 Reducibility

The redox properties of the catalysts have been investigated from H_2-TPR experiments. The profiles of H_2 consumption vs. temperature are presented in Fig. 4. The amount of total hydrogen consumption and reduction temperatures for the peak maximums are given in Table 3. The front side of monolith-A shows the maximum consumption of hydrogen at 76 mmol.g^{-1} while monolith-B is the lowest at 39 mmol.g^{-1}. Noble metals Pd and Rh representing the active species of the catalysts usually reduce below 250 °C depending on the support (washcoat) material influencing the metal-support interactions [33, 34]. Consumption of hydrogen is evident around 65 °C for monolith-A which also shows negative peaks observed commonly for Pd-based zirconia materials as a result of decomposition of palladium hydrides at 75-85 °C formed at the beginning of the reduction process [34-36]. The higher intensity of the negative peak is evident for the front of monolith-A due to heavier Pd loading while an additional peak at 175 °C is observed on the back side most likely due to higher Rh content. The absence of the negative peak in monolith-B can be indirectly indicating that the Pd species are mostly linked to ceria or due to smaller Pd particle sizes [36, 37]. The reduction peaks between 250 and 500 °C can be attributed to the surface reduction of Ce^{4+} species from ceria and/or ceria-zirconia mixed oxides. The reduction temperature as well as the H_2-TPR

profiles can be also to some extent affected by the presence of promoters such as La, Y, Ba etc [36]. The presence of higher loading of noble metals in monolith-A also impacts the reduction peaks arising from the ceria-zirconia based washcoat by shifting to lower temperatures.

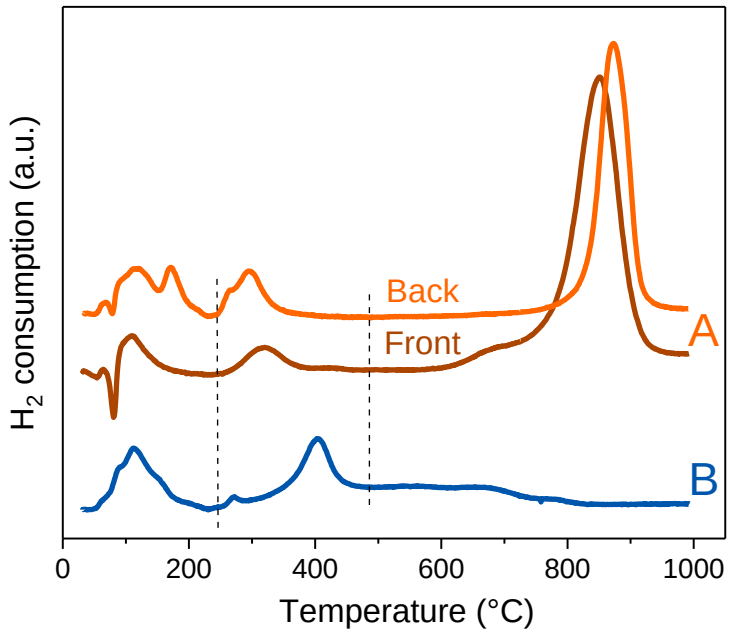

Fig. 4. H_2-TPR profiles of commercial TWCs: monolith-A(front), monolith-A(back) and monolith-B.

Above 500 °C, only monolith-A shows intense peaks appearing due to the bulk reduction of Ce^{4+} species to Ce^{3+}. This is associated with simultaneous formation of $CeAlO_3$, which was verified with an XRD analysis after the TPR analysis given in supplementary material (Figure S6) [37,38]. Such peaks don't appear for monolith-B possibly due to much lower PGM loading such that bulk reduction of ceria happens above the analyzed temperature range. Since only monolith-A contains sulphur, sulphates like $BaSO_4$ can also contribute to the H_2-TPR profile at high temperatures [39,40]. Post-TPR XRD analysis highlights the formation of barium sulfide phase (Figure S6). Thus, it can be established that the intense high temperature peaks formed for monolith-A is a caused by not bulk reduction of Ce^{4+} but also the reduction of the Ba sulfates present.

Table 3. Monolith properties determined from N_2-physisorption and H_2 consumption and reduction peaks from H_2-TPR.

Catalyst	Surface Area BET ($m^2.g^{-1}$)	Total pore volume ($cm^3.g^{-1}$)	H_2 consumption ($mmol.g^{-1}$)	T_{max} of reduction peaks (°C)				
Monolith-A Front	35	0.16	76.31	65.6	82.1	110.1	295.7	848.7
Monolith-A Back	49	0.25	57.36	67.3	78.7	116.8	318.9	873.6
Monolith-B	35	0.15	39.05	-	-	113.5	405.1	-

3.4. Surface properties

3.4.1. Textural properties

The nitrogen isotherms for adsorption-desorption and the BJH pore size distribution of the investigated materials has been displayed in Fig. S3 and the respective specific surface areas and total pore volumes have been given in Table 3. The isotherms of the crushed monoliths show similar behavior to each other showing a type IV isotherm with H3 hysteresis form demonstrating the presence of mesopores [41]. The specific surface area of the monolith-A front side and monolith-B is 35 $m^2.g^{-1}$ and that for monolith-A back side is slightly higher at 49 $m^2.g^{-1}$. Obviously, the total pore volume for monolith-A(back) is the maximum at 25 $cm^3.g^{-1}$. In terms of the pore size distribution, the front and the back side of monolith-A are almost identical with the presence of low diameter mesopores (<5 nm) and the broad peak centered around 21 nm. In case of monolith-B, it has a slightly narrower size distribution with smaller pores centered at around 12 nm. Overall, the commercial monoliths studied here display comparable textural properties likely due to similar preparation methods, in spite of variable oxide compositions.

3.4.2. Surface composition from XPS analysis

The characteristic Ce 3d, Zr 3d, O 1s and Pd 3d (combined with Zr 3p) photopeaks have been analyzed providing information on the valent state and surface composition on a depth of 5-10 nm for each element. The binding energy (BE) values and the related quantification are given in Table 4. The binding energy value for Zr 3d reflects the stabilization of Zr^{4+}. The presence of tetravalent Zr is known to enhance not only the thermal properties but also the bulk oxygen

mobility [11]. The Ce 3d spectra of the investigated catalysts/zones are presented in Fig. S4. The Ce 3d photopeak can be fitted with respect to 10 components among which 4 are attributed to the spin-orbit doublets and the rest to their respective satellites. *u* and *v* correspond to the spin-orbit $3d_{3/2}$ and $3d_{5/2}$ components at a BE of 882.7 and 907.3 eV with an energy separation of 18.6 eV attributed to Ce^{4+} ions. In addition, each show satellite peaks labelled as *v´´, v´´´, u´´* and *u´´´*, respectively. The presence of Ce^{3+} can be easily detected by the position of $3d_{3/2}$ and $3d_{5/2}$ components marked u^0 and v^0 at a BE of 880.9 and 899.1 eV, along with their satellite peaks, *v´* and *u´*, respectively [42]. The spectral decomposition highlights that monolith-B contains maximum Ce^{3+} ions followed by the front and then the back side of monolith-A (Table 4). Higher Ce^{3+}/Ce^{4+} ratio is indicative of higher O-vacancies in monolith-B that could be beneficial for enhancement of the catalytic performance. The O 1s spectra is around 530.1 eV for all the catalysts attributed to the lattice oxygen from metal oxides. The surface oxygen species indicative of the surface oxygen species coincides with contributions from alumina present within the washcoats of each catalyst [43]. Hence, hinders direct comparison between surface and lattice oxygen species. As seen previously, highest Pd content is also evidenced in case of the front side of monolith-A present as a native oxide. The atomic ratios do not match exactly with those obtained from bulk elemental analysis likely due to the high heterogeneity present in the layers of the monolithic samples.

Table 4. The BE values from surface analysis by XPS on the monolithic catalysts and relevant atomic ratios.

Catalyst	**BE Ce 3d**	**BE Zr 3d**	**BE O 1s**	**BE Pd 3d**	**Pd atom.%**	**Ce/Zr ratio**	**Ce^{3+}/Ce^{4+}**
Monolith-A Front	882.6	182.0	530.3	336.8	0.58 /1.85[a]	0.39 /0.38[a]	0.31
Monolith-A Back	882.4	181.9	530.0	336.5	0.10 /0.39[a]	0.39 /0.23[a]	0.23
Monolith-B	882.4	182.1	530.1	336.5	0.06 /0.17[a]	0.37 /0.27[a]	0.38

a From bulk elemental analysis (XRF)

3.5. Catalytic performance evaluation

The aim was to investigate the influence of the PGM content, Ce/Zr ratio and the impact of gradient concentration according to the strategy used for the washcoating on their oxidative

and reductive properties in the course of single and competitive reactions taking place during the engine operation in the temperature range of 100-500 °C with a special attention on low temperature performances (cold start). Accordingly, the single CO oxidation by O_2 and in competition with NO has been investigated. The outlet concentration profiles are illustrated in Fig. 5 and Fig. 7. Regarding propane and propene oxidation by O_2, the corresponding concentration profiles are reported in Fig. 6. As detailed in the experimental section and described in Table S1 and Fig. S2, successive cycles in rich, lean and stoichiometric conditions were preceded for each selected temperature.

3.5.1. Oxidative properties

Let us first examine the evolutions observed on CO concentrations in Fig. 5 and related conversions assigned to the oxidation reaction with O_2. The evolution of the CO concentration during the reaction in case of both monoliths are shown where the richness changes from the rich to lean to stoichiometric regimes under each isothermal step. At the first glance, it is evident that monolith-B shows higher conversion of CO at low temperature of 100 °C, although it is more affected by the variation of the different regimes as compared to monolith-A. At the early stage of the reaction, monolith-B, in spite of its much lower PGM concentration, converts nearly 60% of CO under lean conditions at 100 °C vs. 20% for monolith-A. Another useful information arises by examining the kinetic behavior at 100 °C in lean/rich/stoichiometric conditions. Significant fluctuations occur on the outlet concentration levels recorded on monolith-B, especially in rich conditions corresponding to a significant loss of CO conversion. On the other hand, despite lower performances, the conversion on monolith-A remains quasi unchanged irrespective of the richness. This comparison emphasizes the fact that this latter catalyst would exhibit better OSC properties. Such difference in OSC behavior is still perceptible at 200 °C with an incomplete CO conversion in rich conditions on monolith-B. Further increase in temperature does not lead to discernible changes with a quasi-complete CO conversion irrespective of the operating conditions on both catalysts.

In order to get more insights into the role played by the OSC properties, we have roughly estimated this parameter from our experimental conversion curves by considering the difference between the maximum CO concentration under rich condition (grey line) and the CO remaining unreacted in presence of the TWC catalyst. This difference, or in other words, the CO converted by the catalyst in presence of oxygen is proportional to the OSC of the materials. The calculated OSC values at each temperature with respect to the ceria-zirconia

content in the monoliths are given in Table 5, where the maximum represents the values for full CO conversion under rich conditions. Monolith-A shows higher OSC at all temperatures in comparison to monolith-B, which does not reach the maximum even at 400-500 °C. The estimated OSC were compared to those obtained from O_2 temperature programmed desorption analysis in Table 5. Similar values support the evolutions of the conversion observed on both catalysts explaining the magnitude of CO conversion on monolith-B according to the richness.

The higher oxygen storage capacity exhibited by monolith-A is in good agreement with the higher amount of cerium. Improved OSC properties could be also related to the formation of $Ce_xZr_{1-x}O_2$ solid solutions [23]. Unfortunately, such hypothesis is not directly supported by XRD analysis. On the other, it could be partly supported by SEM-EDX analysis based on the observation of homogeneous distributions of Ce and Zr across the washcoat of monolith-B. In such case, the lower Ce/Zr ratio observed on sample should lead to a preferential tetragonal Zr-rich $Ce_xZr_{1-x}O_2$ structure characterized by a lower oxygen mobility compared to a cubic structure [44]. On the contrary, the presence of significant heterogeneities in monolith-A associated with the formation of CeO_2 aggregates could be more favorable in terms of surface oxygen mobility. Such an interpretation seems consistent with H_2-TPR measurements which shows that surface reduction processes occur more readily on monolith-A than on monolith-B.

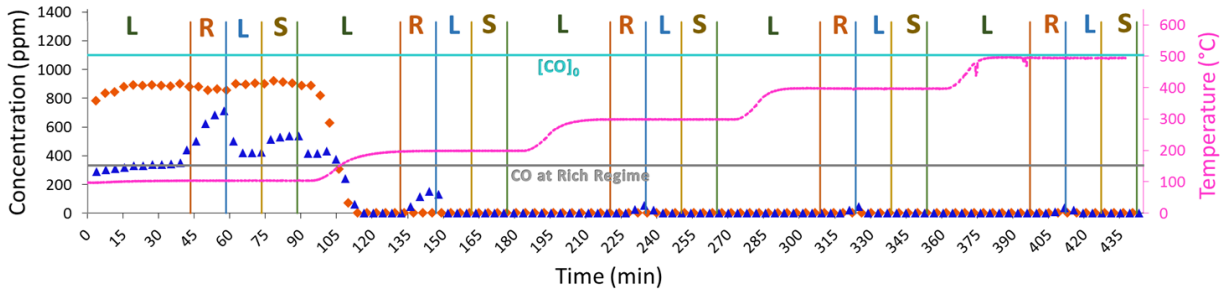

Fig. 5. Evolution of CO concentration with time during temperature-programmed CO oxidation reaction with monolith-A (orange diamonds) and monolith-B (blue triangles) under rich (R), lean (L) and stoichiometric (S) conditions at each 100 °C. The horizontal light blue solid line $[CO]_0$ refers to the initial CO concentration and the horizontal grey solid line represents the theoretical CO concentration that should remain not converted due to lower O_2 supply ($\lambda = 1.5$) in the gas phase under rich conditions.

Table 5. Estimated OSC values from experimental data with respect to the ceria-zirconia content in monolith-A and monolith-B.

Catalyst	OSC (µmol $O_2.g^{-1}_{ceria\text{-}zirconia}$)					O_2-TPD[#] ($\mu mol.\ g^{-1}$)
	200 °C	300 °C	400 °C	500 °C	Maximum*	
A	42.1	42.1	42.1	42.1	42.1	43.6
B	31.7	42.5	43.7	43.7	45.3	43.4

*To convert the excess of CO

[#] Room temperature to 1000 °C

As expected the reactivity of propane is much lower (see Fig. 6) with a significant delay in conversion compared to propene and CO. The estimation of the temperature at half conversion of 146 °C and 180 °C for propene and of 280 °C and 304 °C for propane on monolith-A and B, respectively, clearly emphasize the superiority of monolith-A whereas monolith B is obviously more active for CO. It is also worthwhile to note that propene conversion at low temperature seems to be sensitive to the richness without distinction. Indeed, lean conditions promote the conversion of propene whereas rich conditions have a strong detrimental effect. For propane this effect is less pronounced suggesting that OSC properties improve at higher temperature. Such tendency emphasizes a more appropriate design for monolith-A containing high amount of palladium in the front side which could benefit the oxidation of more refractory alkanes.

The possible presence of sulphate in monolith-A seems to have no detrimental impact. The role of sulphate in oxidative properties is unclear because it could *a priori* suppress oxygen mobility of ceria. However, SEM-EDX and H_2-TPR experiments seem to indicate that preferential interactions take place more likely with barium through the formation of barium sulphate. Some studies claim that small amount of sulfur could enhance HC oxidation especially for alumina containing TWC catalysts and also reduce coking effect to some extent under rich conditions [30, 31].

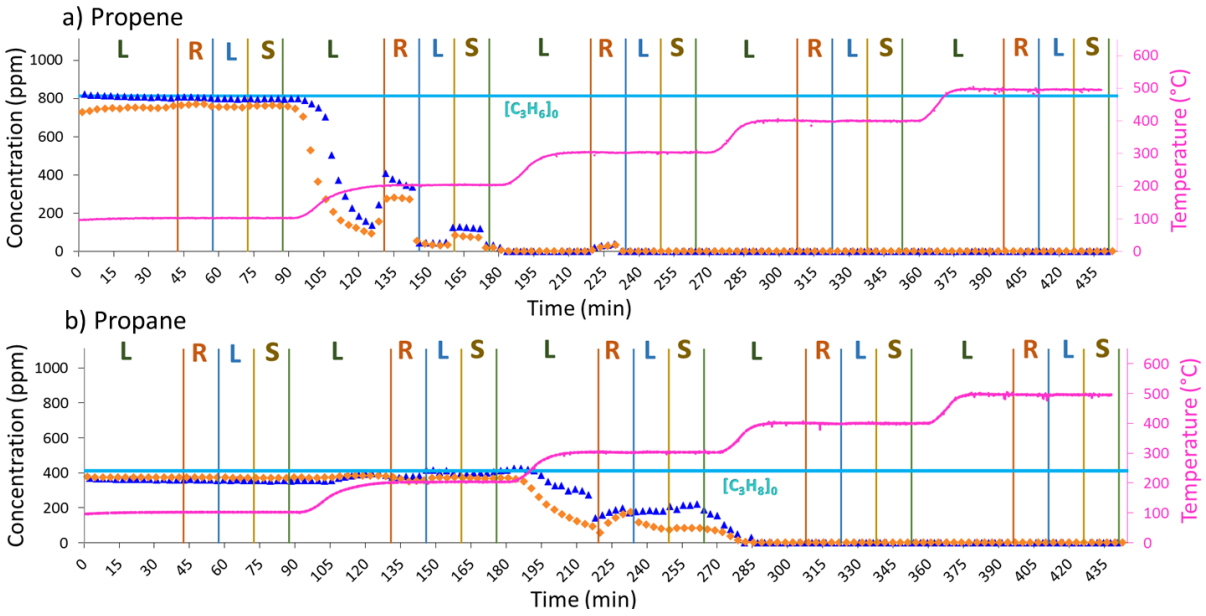

Fig. 6. Evolution of a) propene and b) propane concentration with time during temperature-programmed C_3H_6/C_3H_8 oxidation reaction with monolith-A (orange diamonds) and monolith-B (blue triangles) under rich (R), lean (L) and stoichiometric (S) conditions at each 100 °C.

3.5.2. CO/NO reaction

In the presence of oxygen in the CO/NO gas mixture (see Table S1 in SI) the CO/O_2 and CO/NO reactions will compete. The formation of NO_2 from NO oxidation has not been detected in the whole range of our operating conditions. Consequently, the conversion of NO and the production of N_2 and N_2O merely reflect the reductive properties of monolith-A and B. Accordingly, Eqs. (1)-(3) illustrate the predominant reactions taking place over these two catalysts:

$$2CO + O_2 \rightarrow 2CO_2 \quad (1)$$

$$CO + 2NO \rightarrow N_2O + CO_2 \quad (2)$$

$$2CO + 2NO \rightarrow N_2 + CO_2 \quad (3)$$

$$CO + N_2O \rightarrow N_2 + CO_2 \quad (4)$$

By examining Fig. 7(a) intriguing observations arise at 100°C because the concentration profiles for CO are superimposed and a weak sensibility of the richness is discernible on monolith-B contrary to Fig. 5. Clearly, NO adsorption on monolith-B would strongly inhibit

the rate of CO/O_2 reaction. On the other hand, further increase in temperature leads to the complete CO conversion similar to Fig. 5. As a general trend presented in Fig. 8, the examination of NO conversion profiles jointly with N_2O production clearly indicate that N_2O formation is more favored at low temperature and in lean and stoichiometric conditions and then decreases after switching to the rich condition. Successive N_2O reduction takes place with a rise in NO conversion in accordance with Eq. (4) and seems to be responsible for the selective production of nitrogen at high temperature. Such tendency is more accentuated on monolith-A which strongly outperforms monolith-B in terms of NO conversion and selectivity towards the production of N_2.

It appears that these evolutions are mostly governed by the competition between NO reduction by CO and CO oxidation by O_2. Clearly this competition is in favor of NO reduction in rich conditions. On the other hand, the CO/O_2 reaction becomes predominant with a rise in temperature mainly in lean conditions. Obviously, monolith-B becomes ineffective towards NO reduction above 400°C except in rich conditions. Indeed, a complete disappearance of NO conversion is evidenced. Such an observation agrees with a faster CO oxidation by O_2 on monolith-B as shown in Fig. 5. On the other hand, the performances of monolith-A in the CO/NO reaction are less affected by the rise in temperature preserving NO conversion above 50% in lean conditions associated to a complete production of nitrogen. The superiority of monolith-A in the CO/NO reaction can be related to the presence of higher amount of palladium and likely higher amount of Rh in the back side compared to monolith-B, i.e. 0.07% Rh instead of 0.03% Rh. Accordingly, NO likely dissociates more readily on Rh than on Pd which could be responsible of higher NO conversion level compared to monolith-B. As the consequence, a significant residual production of N_2O (>20 ppm) occurs on monolith-B probably because the successive reduction of N_2O would also occur more slowly. Such peculiar behavior is usually assigned to a strong NO adsorption preventing N_2O re-adsorption. Hence, a faster NO dissociation at low temperature on monolith-A could be a crucial parameter preventing high NO coverage and subsequent inhibiting effect. Such a beneficial outcome could be accentuated by the proximity of Rh-sites with anionic vacancies from ceria [47]. Such an assumption seems reasonably acceptable by examining the Ce/Zr ratio as well as the significant Ce^{3+}/Ce^{4+} ratio.

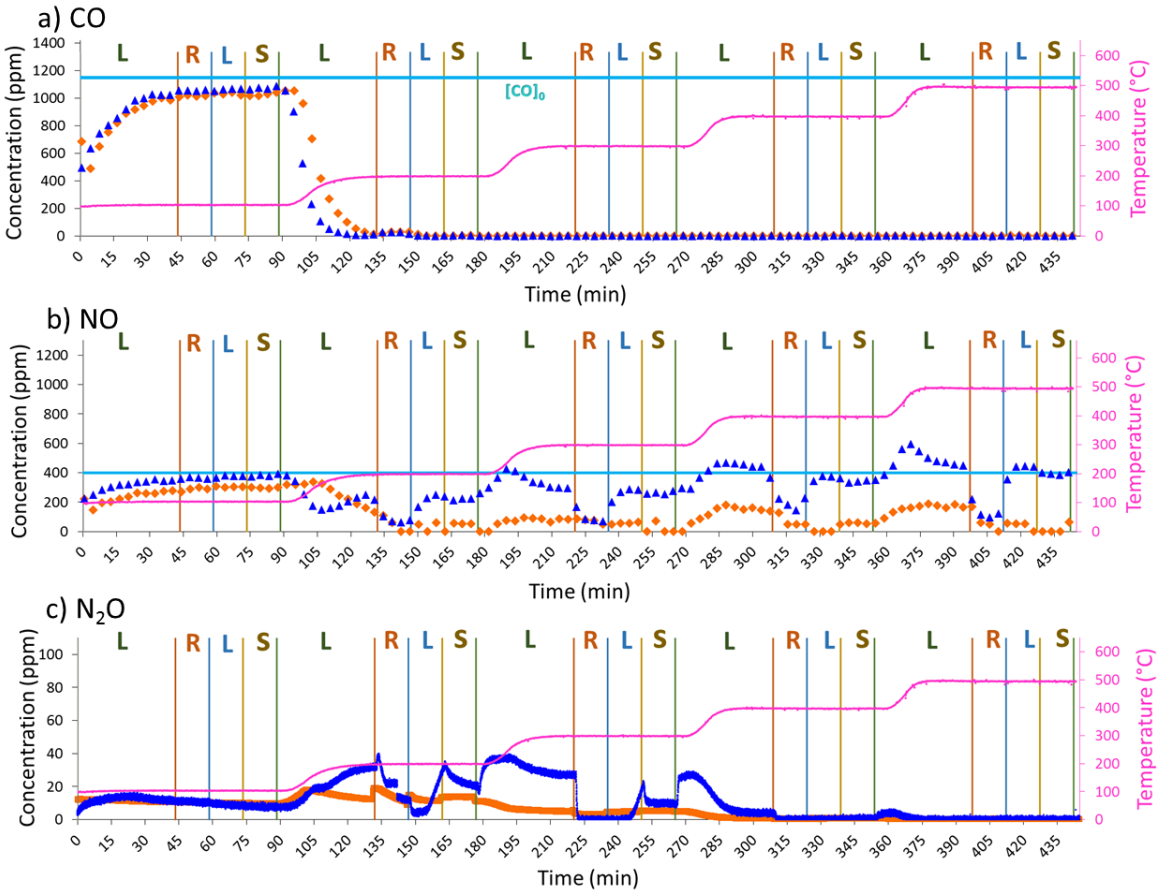

Fig. 7. Evolution of a) CO, b) NO and c) N_2O concentration with time during temperature-programmed CO/NO oxidation reaction with monolith-A (orange diamonds) and monolith-B (blue triangles) under rich (R), lean (L) and stoichiometric (S) conditions at each 100 °C.

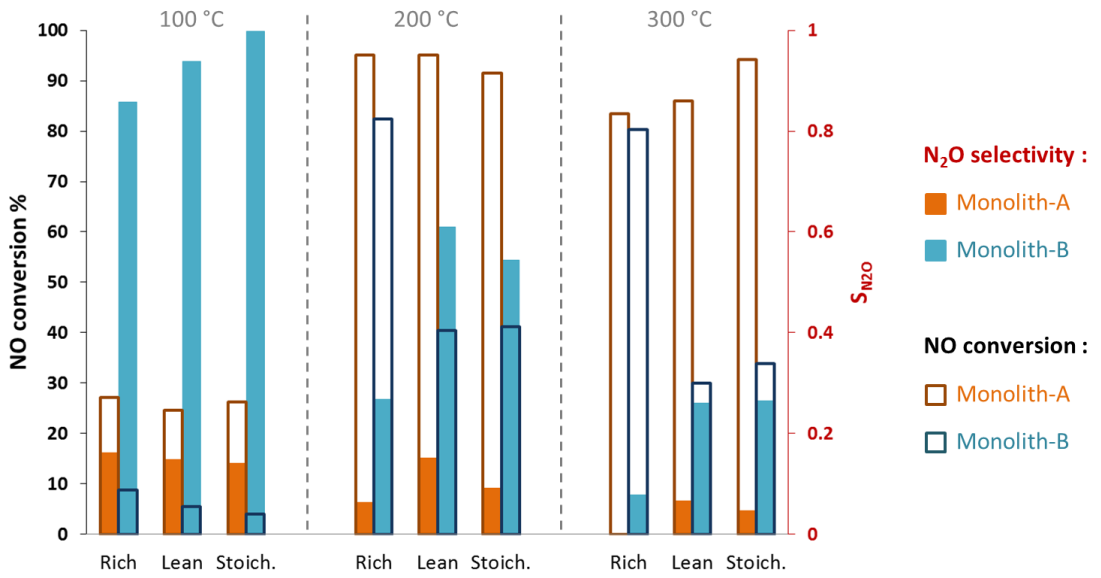

Fig. 8. Comparison of N_2O selectivity (filled bars) and NO conversion (open bars) from 100°C to 300°C under rich/lean/stoichiometric conditions for monolith-A (orange) and monolith-B (blue).

3.6. General assessment

In this work, the systematic comparison between the commercial TWCs: monolith-A and monolith-B, highlighted numerous differences in the manufacturing strategies adapted by the automotive manufacturers. This makes it highly complex to directly predict the origin of the catalytic performances. Yet, this study elucidates important information about the current TWC technology in use on the roadways worldwide. Monolith-A has been prepared following a complex route with incorporation of zoning having differential concentration of the noble metals and other trace elements. It consists of as high as 1.85% / 0.39% of Pd and 0.01% / 0.07% of Rh on the front and back side, respectively. The front side mainly aims to ensure the CO removal while the back side is dedicated to NO_x abatement. However, other authors have reported that a higher Pd loading in TWC catalysts did not significantly improve the catalytic performance for HC and NO_x removal, although increasing the Rh loading helped in improving the activity [42-43]. Since Pd strongly adsorbs CO making it a rate-limiting step [4], higher loading of Pd may increase significantly the total cost of the catalyst for "in fine" limited benefits. Nevertheless, introducing a high amount of Pd in front of the catalyst could also have a cooperative effect to increase the overall temperature of the material due to higher exothermic HC conversion with the ultimate goal of improving NOx to N_2 reduction, thus avoiding N_2O formation. Indeed, slightly higher performances for HC (propane and propene) oxidation was observed for zoned monolith-A as well as lower N_2O selectivity. Although a poor low temperature CO oxidation activity is reported in this case, the enhanced NO reduction performances by CO is also supported by the high Rh-loading on the back side of monolith-A similar to the observations in literature [49]. Higher concentration of dopants like La and Y with additional presence of S and Pr is also evidenced. The manufacturing cost is thereby substantially increased due to this zoning methodology, higher levels of trace dopants and PGM content. This strategy mainly enabled to improve NO_x removal by CO and CO oxidation performances with oxygen under rich conditions above 200 °C by providing enhanced OSC properties. However, no significant increase in the HC oxidation and poor low temperature CO removal by oxygen are observed, important for cold-start conditions. Thus, in a context where most of car manufacturers are looking for decreasing PGMs loading, one could consider the high price point of monolith-A as a disputable choice with respect to its performance up to a certain extent.

In contrast, monolith B is homogeneously prepared with regular Al/Ce/Zr oxide mixture, lower PGM content with 0.16% Pd, 0.03% Rh and other dopants. Still this less expensive catalyst shows better CO conversion especially at low temperatures and similar CO oxidation

performance with NO as that of monolith-A. However, this catalyst is highly impacted by the fluctuation of the regimes in temperature ranges up to 500°C. Moreover, the NO reduction is limited most likely due to lower Rh loading with high N_2O formation. The formation of the latter, especially under 300 °C is a challenging issue in terms of catalytic converter performances during cold start of vehicle engines. Indeed, N_2O is considered 310 times more harmful for the destruction of ozone layer than CO_2. Next European regulations might probably restrict the N_2O emissions leading automotive industries to develop more efficient catalysts at low temperature or use alternative pre-heating systems. According to a report from Johnson Matthey, cost savings can be efficiently done by decreasing the Pd (or Pt) levels and not Rh loadings as it helps to boost TWC performances [49]. A better attention should also be put on the preparation of washcoat oxides, physically blended or co-precipitated, to increase thermal stability and OSC performances at low temperature.

Therefore, to improve the cost effectiveness of TWC catalyst manufacturing, optimization of the key parameters such as PGM loading, OSC, S concentration etc. is necessary to achieve the best conversion efficiencies while reducing the price and stabilize the social-economic issues related to PGM usage. Future challenge will be also to increase the catalytic performances at low-temperature in response to the cold-start emission issue from thermal and hybrid engines.

4. Conclusion

Two commercial TWC catalysts shaped as monoliths, currently being used by major car companies were investigated to examine the current TWC technology and their fabrication strategies. The main finding was based on the fact that cost-performance relationship plays the primary role in making judicious choice of the catalyst composition. In this study, both catalysts consisted of a ceramic cordierite support having double-washcoated layers with complex composition based on ceria-zirconia and alumina. Other trace elements in varying amounts across the two monoliths were also detected such as La, Y, Nd, Pr, Ba and even S to enhance different catalyst properties. Monolith-A had a much higher precious metal loading and extra dopants manufactured with the length-wise zoning methodology with separate Pd and Rh-rich zones for facilitating CO/HC oxidation and NO_x reduction, respectively. However, this unexpectedly did not improve the catalytic performance substantially with respect to CO and HC oxidation, especially at low temperatures. Nevertheless, monolith-A top washcoat layer comprised of alumina blended with cerium-enriched ceria/zirconia particles develop better oxygen storage capacity especially appreciated during rich regimes to

convert CO. Characterization experiments seems to indicate the presence Ba sulfates in monolith-A whose usefulness remains rather limited or even unfavorable for catalytic performances. On the other hand, monolith-B irrespective of its lower Pd levels performed better under cold-start conditions for CO oxidation. Only NO_x removal was considerably lower accompanied by increased N_2O selectivity owing to low Rh doping compared to monolith-A. Moreover, the washcoat top surface was composed of Zr-enriched ceria/zirconia with alumina particles negatively affecting the oxygen mobility in the catalysts.

The results on the characterization and catalytic reaction evaluation will provide directions to not only better optimize the dopants/PGM concentration but also choose the correct strategy for further development of TWC keeping in mind the necessity of lowering PGM and critical raw materials content as well as cold start emission and new Euro 7 (N_2O, NH_3, CH_4) pollutant abatement in a cost-effective manner in future.

Sample CRediT author statement

S. Nandi: Investigation, Validation, Visualization, Formal analysis Writing - Original Draft ; **P. Arango:** Methodology, Investigation, Writing - Review & Editing ; **C. Chaillou:** Conceptualization, Funding acquisition, Validation ,Writing - Review & Editing ; **C. Dujardin:** Supervision, Methodology, Resources, Validation, Writing - Review & Editing, **P. Granger:** Supervision, Validation, Writing - Review & Editing ; **E. Laigle:** Validation, Writing - Review & Editing ; **A. Nicolle:** Conceptualization, Validation, Writing - Review & Editing ; **C. Norsic:** Conceptualization, Project administration, Supervision, Validation, Writing - Review & Editing ; **M. Richard:** Supervision, Methodology, Validation, Visualization, Writing - Original Draft, Review & Editing.

Declaration of interests

The authors declare that they have no known competing financial interests or personal relationships that could have appeared to influence the work reported in this paper.

Acknowledgements

The FEDER, the CNRS, the Région Nord Pas-de-Calais and the Ministère de l'Education Nationale de l'Enseignement Supérieur et de la Recherche are acknowledged for fundings of XPS/LEIS/ToF-SIMS spectrometers within the Pôle Régional d'Analyses de Surface and X-ray diffractometers. The authors would like to acknowledge Laurence Burylo, Nora Djelal, Olivier Gardoll, Romain Jooris, Stephane Lebrun, Pardis Simon and Maxence Vandewalle for their assistance in characterization experiments.

Funding

This work was supported by ARAMCO Company.

ORCID numbers

S. Nandi: 0000-0002-5904-0539
P. Arango: 0000-0002-3721-7954
C. Chaillou: 0000-0001-5292-7463
C. Dujardin: 0000-0001-8266-0165
P. Granger: 0000-0002-8333-4246
E. Laigle: 0000-0003-4951-083X
C. Norsic: 0000-0002-6904-4509
M. Richard: 0000-0001-6789-6997

References

[1] World Health Organization, Air Quality Guidelines: Global Update 2005 : Particulate Matter, Ozone, Nitrogen Dioxide, and Sulfur Dioxide, World Health Organization (2006).

[2] R.J. Farrauto, M. Deeba, S. Alerasool, Gasoline automobile catalysis and its historical journey to cleaner air, Nat. Catal. 2 (2019) 603–613.

[3] S. Rood, S. Eslava, A. Manigrasso, C. Bannister, Recent advances in gasoline three-way catalyst formulation: A review, Proc. Inst. Mech. Eng. Part D J. Automob. Eng. 234 (2020) 936–949.

[4] A. Martínez-Arias, M. Fernández-García, A.B. Hungría, A. Iglesias-Juez, K. Duncan, R. Smith, J.A. Anderson, J.C. Conesa, J. Soria, Effect of thermal sintering on light-off performance of Pd/(Ce, Zr)Ox/Al2O3 three-way catalysts: Model gas and engine tests, J. Catal. 204 (2001) 238–248.

[5] I. Nova, B. Epling, C. Peden, Challenges for catalytic exhaust aftertreatment, Catal. Today. 231 (2014) 1–2.

[6] M.P. González-Marcos, B. Pereda-Ayo, A. Aranzabal, J.A. González-Marcos, J.R. González-Velasco, On the effect of reduction and ageing on the TWC activity of Pd/Ce 0.68Zr 0.32O 2 under simulated automotive exhausts, Catal. Today. 180 (2012) 88–95.

[7] S. Bedrane, C. Descorme, D. Duprez, Investigation of the oxygen storage process on ceria- and ceria-zirconia-supported catalysts, Catal. Today. (2002) 401–405.

[8] M. Sugiura, Oxygen storage materials for automotive catalysts: Ceria-zirconia solid solutions, Catal. Surv. from Asia. 7 (2003) 77–87.

[9] M. Ozawa, M. Hattori, T. Yamaguchi, Thermal stability of ceria catalyst on alumina and its surface oxygen storage capacity, J. Alloys Compd. 451 (2008) 621–623.

[10] T. Montini, M. Melchionna, M. Monai, P. Fornasiero, Fundamentals and Catalytic Applications of CeO2-Based Materials, Chem. Rev. 116 (2016) 5987–6041.

[11] P. Li, X. Chen, Y. Li, J.W. Schwank, A review on oxygen storage capacity of CeO 2 - based materials: Influence factors, measurement techniques, and applications in reactions related to catalytic automotive emissions control, Catal. Today. 327 (2019) 90–115.

[12] W. Lang, P. Laing, Y. Cheng, C. Hubbard, M.P. Harold, Co-oxidation of CO and propylene on Pd/CeO2-ZrO2 and Pd/Al2O3 monolith catalysts: A light-off, kinetics, and mechanistic study, Appl. Catal. B Environ. 218 (2017) 430–442.

[13] A. Papavasiliou, A. Tsetsekou, V. Matsouka, M. Konsolakis, I. V. Yentekakis, An investigation of the role of Zr and La dopants into Ce1-x-yZrxLayOδ enriched γ-Al2O3 TWC washcoats, Appl. Catal. A Gen. 382 (2010) 73–84.

[14] Q. Wang, B. Zhao, G. Li, R. Zhou, Application of rare earth modified Zr-based ceria-zirconia solid solution in three-way catalyst for automotive emission control, Environ. Sci. Technol. 44 (2010) 3870–3875.

[15] J. Guo, M. Gong, S. Yuan, Y. Chen, Effect of BaO on catalytic activity of Pt-Rh TWC, J. Rare Earths. 24 (2006) 554–559.

[16] B. Zhao, Q. Wang, G. Li, R. Zhou, Effect of rare earth (La, Nd, Pr, Sm and Y) on the performance of Pd/Ce0.67Zr0.33MO2-δ three-way catalysts, J. Environ. Chem. Eng. 1 (2013) 534–543.

[17] M. Haneda, Y. Tomida, H. Sawada, M. Hattori, Effect of Rare Earth Additives on the Catalytic Performance of Rh/ZrO2 Three-Way Catalyst, Top. Catal. 59 (2016) 1059–1064.

[18] S. Govender, H. Friedrich, Monoliths: A Review of the Basics, Preparation Methods and Their Relevance to Oxidation, Catalysts. 7 (2017) 62.

[19] H. Chang, H. Chen, K. Koo, J. Rieck, Gasoline Cold Start Concept (gCSC^{TM}) Technology for Low Temperature Emission Control, SAE Int. J. Fuels Lubr. 7 (2014) 480–488.

[20] J.Y. Favez, M. Weilenmann, J. Stilli, Cold start extra emissions as a function of engine stop time: Evolution over the last 10 years, Atmos. Environ. 43 (2009) 996–1007.

[21] J. Li, X. Liu, W. Zhan, Y. Guo, Y. Guo, G. Lu, Preparation of high oxygen storage capacity and thermally stable ceria-zirconia solid solution, Catal. Sci. Technol. 6 (2016) 897–907.

[22] A.A. Vedyagin, V.O. Stoyanovskii, P.E. Plyusnin, Y. V. Shubin, E.M. Slavinskaya, I. V. Mishakov, Effect of metal ratio in alumina-supported Pd-Rh nanoalloys on its performance in three way catalysis, J. Alloys Compd. 749 (2018) 155–162.

[23] J. Wu, A. Glisenti, J.P. Dacquin, C. Dujardin, C. Fernández Acevedo, C. Salazar Castro, P. Granger, CexZr1−xO2 mixed oxide as OSC materials for supported Pd three-way catalysts: Flame-spray-pyrolysis vs. co-precipitation, Appl. Catal. A Gen. 598 (2020) 117527.

[24] J. Wang, H. Chen, Z. Hu, M. Yao, Y. Li, A review on the Pd-based three-way catalyst, Catal. Rev. - Sci. Eng. 57 (2015) 79–144.

[25] Hai-Ying Chen, H.-L. Chang, Development of Low Temperature Three-Way Catalysts for Future Fuel Effi cient Vehicles Novel alumina/ceria/zirconia mixed oxide with improved thermal stability and oxygen storage capacity enhances low temperature performance of three-way catalysts, Johnson Matthey Technol. Rev. (2015) 64–67.

[26] A. Suda, K. Yamamura, Y. Ukyo, T. Sasaki, H. Sobukawa, T. Tanabe, Y. Nagai, M. Sugiura, Effect of Specific Surface Area of Ceria-Zirconia Solid Solutions on Their Oxygen Storage Capacity, J. Ceram. Soc. Japan. 112 (2004) 581–585.

[27] E. Rohart, V. Bellière-Baca, K. Yokota, V. Harlé, C. Pitois, Rare earths based oxides as alternative materials to Ba in NOx-trap catalysts, Top. Catal. (2007) 71–75.

[28] R. Si, Y.W. Zhang, L.M. Wang, S.J. Li, B.X. Lin, W.S. Chu, Z.Y. Wu, C.H. Yan, Enhanced thermal stability and oxygen storage capacity for Ce xZr1-xO2 (x = 0.4-0.6) solid solutions by hydrothermally homogenous doping of trivalent rare earths, J. Phys. Chem. C. 111 (2007) 787–794.

[29] L. Yang, X. Yang, S. Lin, R. Zhou, Insights into the role of a structural promoter (Ba) in three-way catalyst Pd/CeO2-ZrO2 using in situ DRIFTS, Catal. Sci. Technol. 5 (2015) 2688–2695.

[30] L. Lan, S. Chen, Y. Cao, S. Wang, Q. Wu, Y. Zhou, M. Huang, M. Gong, Y. Chen, Promotion of CeO2-ZrO2-Al2O3 composite by selective doping with barium and its supported Pd-only three-way catalyst, J. Mol. Catal. A Chem. 410 (2015) 100–109.

[31] T.S. Rodrigues, F.A. e Silva, E.G. Candido, A.G.M. da Silva, R. dos Rafael, P.H.C. Camargo, M. Linardi, F.C. Fonseca, Ethanol steam reforming: understanding changes in the activity and stability of Rh/M xO y catalysts as function of the support, J. Mater. Sci. 54 (2019) 11400–11416.

[32] J. Jin, C. Li, C.W. Tsang, B. Xu, C. Liang, Catalytic combustion of methane over Pd/Ce-Zr oxides washcoated monolithic catalysts under oxygen lean conditions, RSC Adv. 5 (2015) 102147–102156.

[33] S. Bhogeswararao, D. Srinivas, Catalytic conversion of furfural to industrial chemicals over supported Pt and Pd catalysts, J. Catal. 327 (2015) 65–77.

[34] X. Li, H. Su, G. Ren, S. Wang, A highly stable Pd/SiO2/cordierite monolith catalyst for 2-ethyl-anthraquinone hydrogenation, RSC Adv. 5 (2015) 100968–100977.

[35] A. Benedetti, G. Fagherazzi, F. Pinna, G. Rampazzo, M. Selva, G. Strukul, The influence of a second metal component (Cu, Sn, Fe) on Pd/SiO2 activity in the hydrogenation of 2,4-dinitrotoluene, Catal. Letters. 10 (1991) 215–223.

[36] X. Wang, G. Lu, Y. Guo, L. Jiang, Y. Guo, C. Li, Effect of additives on the structure characteristics, thermal stability, reducibility and catalytic activity of CeO2-ZrO2 solid solution for methane combustion, J. Mater. Sci. 44 (2009) 1294–1301.

[37] H.C. Yao, Y.F.Y. Yao, Ceria in automotive exhaust catalysts. I. Oxygen storage, J. Catal. 86 (1984) 254–265.

[38] A.I. Kozlov, H.K. Do, A. Yezerets, P. Andersen, H.H. Kung, M.C. Kung, Effect of preparation method and redox treatment on the reducibility and structure of supported ceria-zirconia mixed oxide, J. Catal. 209 (2002) 417–426.

[39] M.A. Gómez-García, V. Pitchon, A. Kiennemann, Pollution by nitrogen oxides: An approach to NOx abatement by using sorbing catalytic materials, Environ. Int. 31 (2005) 445–467.

[40] S. Elbouazzaoui, X. Courtois, P. Marecot, D. Duprez, Characterisation by TPR, XRD and NOx storage capacity measurements of the ageing by thermal treatment and SO2 poisoning of a Pt/Ba/Al NOx-trap model catalyst, Top. Catal. (2004) 493–496.

[41] M. Thommes, K. Kaneko, A. V. Neimark, J.P. Olivier, F. Rodriguez-Reinoso, J. Rouquerol, K.S.W. Sing, Physisorption of gases, with special reference to the evaluation of surface area and pore size distribution (IUPAC Technical Report), Pure Appl. Chem. 87 (2015) 1051–1069.

[42] E. Bêche, P. Charvin, D. Perarnau, S. Abanades, G. Flamant, Ce 3d XPS investigation of cerium oxides and mixed cerium oxide (Ce xTiyOz), Surf. Interface Anal.(2008) 264–267.

[43] H. Nohira, W. Tsai, W. Besling, E. Young, J. Petry, T. Conard, W. Vandervorst, S. De Gendt, M. Heyns, J. Maes, M. Tuominen, Characterization of ALCVD-Al2O3 and ZrO2 layer using X-ray photoelectron spectroscopy, J. Non. Cryst. Solids. 303 (2002) 83–87.

[44] S.A. Ghom, C. Zamani, S. Nazarpour, T. Andreu, J.R. Morante, Oxygen sensing with mesoporous ceria-zirconia solid solutions, Sensors Actuators, B Chem. 140 (2009) 216–221.

[45] R. Burch, E. Halpin, M. Hayes, K. Ruth, J.A. Sullivan, The nature of activity enhancement for propane oxidation over supported Pt catalysts exposed to sulphur dioxide, Appl. Catal. B Environ. 19 (1998) 199–207.

[46] Y. Deng, T.G. Nevell, R.J. Ewen, C.L. Honeybourne, Sulfur poisoning, recovery and related phenomena over supported palladium, rhodium and iridium catalysts for methane oxidation, Appl. Catal. A, Gen. 101 (1993) 51–62.

[47] P. Granger, L. Delannoy, J.J. Lecomte, C. Dathy, H. Praliaud, L. Leclercq, G. Leclercq,

Kinetics of the CO + NO reaction over bimetallic platinum-rhodium on alumina: Effect of ceria incorporation into noble metals, J. Catal. 207 (2002) 202–212.

[48] E.A. Alikin, A.A. Vedyagin, High Temperature Interaction of Rhodium with Oxygen Storage Component in Three-Way Catalysts, Top. Catal. 59 (2016) 1033–1038.

[49] J.Cooper and J.Beecham, A study of platinum group metals in three-way autocatalysts., Platin. Met. Rev. 57 (2013) 57–281.